

See discussions, stats, and author profiles for this publication at: <https://www.researchgate.net/publication/273342936>

Physiochemical Investigation of Shape Designed MnO₂ Nanostructures and Their Influence on Oxygen Reduction Reaction Activity in Alkaline Solution

ARTICLE *in* THE JOURNAL OF PHYSICAL CHEMISTRY C · MARCH 2015

Impact Factor: 4.77

READS

99

8 AUTHORS, INCLUDING:



Senthil Kumar S. M.

Central Electrochemical Research Institute

28 PUBLICATIONS 568 CITATIONS

[SEE PROFILE](#)



Thangamuthu Rangasamy

Central Electrochemical Research Institute

56 PUBLICATIONS 588 CITATIONS

[SEE PROFILE](#)



Parasmani Rajput

Bhabha Atomic Research Centre

46 PUBLICATIONS 217 CITATIONS

[SEE PROFILE](#)



D. Bhattacharyya

Bhabha Atomic Research Centre

166 PUBLICATIONS 1,262 CITATIONS

[SEE PROFILE](#)

Physiochemical Investigation of Shape-Designed MnO₂ Nanostructures and Their Influence on Oxygen Reduction Reaction Activity in Alkaline Solution

Karuppiah Selvakumar,[†] Sakkarapalayam Murugesan Senthil Kumar,^{*,†} Rangasamy Thangamuthu,[†] Kruthika Ganesan,[‡] Palanichamy Murugan,[‡] Parasmani Rajput,[§] Shambhu Nath Jha,[§] and Dibyendu Bhattacharyya[§]

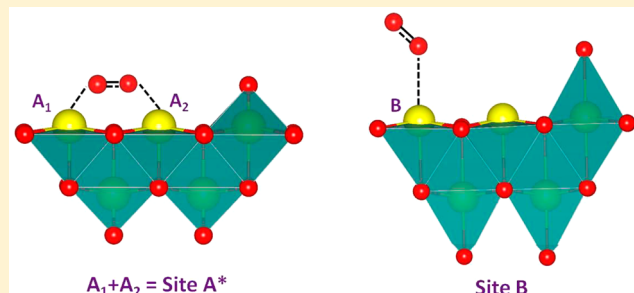
[†]Electrochemical Materials Science Division, CSIR-Central Electrochemical Research Institute, Karaikudi, Tamil Nadu 630 006, India

[‡]Functional Materials Division, CSIR-Central Electrochemical Research Institute, Karaikudi, Tamil Nadu 630 006, India

[§]Atomic & Molecular Physics Division, Bhabha Atomic Research Centre, Trombay, Mumbai 400 085, India

S Supporting Information

ABSTRACT: In this work, five types of MnO₂ nanostructures (nanowires, nanotubes, nanoparticles, nanorods, and nanoflowers) were synthesized with a fine control over their α -crystallographic form by hydrothermal method. The electrocatalytic activities of these materials were examined toward oxygen reduction reaction (ORR) in alkaline medium. Numerous characterizations were correlated with the observed activity by analyzing their crystal structure (TGA, XRD, TEM), material morphology (FE-SEM), porosity (BET), inherent structural nature (IR, Raman, ESR), surfaces (XPS), and electrochemical properties (Tafel, Koutecky–Levich plots and % of H₂O₂ produced). Moreover, X-ray absorption near-edge structure (XANES) and the extended X-ray absorption fine structure (EXAFS) analysis were employed to study the structural information on the MnO₂ coordination number as well as interatomic distance. These combined results show that the electrocatalytic activities are significantly dependent on the nanoshapes and follow an order nanowire > nanorod > nanotube > nanoparticle > nanoflower. α -MnO₂ nanowires possess enhanced electrocatalytic activity compared to other shapes, even though the nanotubes possess a much higher BET surface area. In the ORR studies, α -MnO₂ nanowires displayed Tafel slope of 65 mV/decade, n-value of 3.5 and 3.6% of hydrogen peroxide production. The superior ORR activity was attributed to the fact that it possesses active sites composed with two shortened Mn–O bonds along with a Mn–Mn distance of 2.824 Å, which provides an optimum requirement for the adsorbed oxygen in a bridge mode favoring the direct 4 electron reduction. In accordance with the first principles based density functional theory (DFT), the enhancement in ORR activity is due to the less activation energy needed for the reaction by the (211) surface than all other surfaces.



INTRODUCTION

The oxygen reduction reaction (ORR) is considered as one of the most important electrochemical reaction with respect to its tremendous applications in green energy conversion/storage systems ranging from fuel cells to metal/air batteries.^{1–5} Until now, materials containing precious metals such as platinum, palladium, and gold are the most successful electrocatalysts for the above said ORR.^{3,6–9} The high costs and scarcity of the requisite raw materials have hampered large-scale commercial applications. This has led to an urgent need for electrocatalyst composed of low-cost and more abundant materials but with equal or comparable activity to precious-metal-based electrocatalysts. Indeed, various non-noble materials, such as carbon, polymer, transition metal oxides, like, MnO₂ and Co₂O₃, have been suggested as alternative electrocatalysts for the ORR.^{1,2,4,10,11} Among them, manganese oxides have drawn

particular attention because of their low cost, high activity in alkaline media, and they are environmentally benign.^{12–20} In connection with this, a successful prototype rechargeable Li/O₂ battery by employing α -MnO₂ nanowires has been developed and demonstrated by Bruce and co-workers that it can deliver a much higher capacity than conventional intercalation type lithium batteries.²¹ Similarly in another report, Zhuang and his team have developed a high-performance OH[–] conductive polymer and adopted it to construct an efficient prototype of a non-noble metal-based alkaline polymer electrolyte fuel cell (APEFC).²²

Received: December 23, 2014

Revised: March 5, 2015

Published: March 5, 2015

Despite insufficient stability in acidic media, MnO_2 can be applied as an alternate and promising catalyst in air electrode for both alkaline fuel cells and metal air batteries. For example, MnO_x particles doped with transition metal ions, like, Ca(II), Mg(II), Ni(II), Bi(III), and Cr(III) exhibited ORR specific activities close to the benchmark Pt/C catalyst.²³ Mn_3O_4 nanoparticles loaded on mesoporous carbon also showed high ORR electrocatalytic performance.¹⁴ The catalytic activity toward ORR in alkaline electrolyte results from the oxygen-containing groups and the redox reactions.^{16,24–29} However, uncertainty about the ORR mechanism on MnO_x still remains because of the complex chemistry among Mn species that possess different valence and crystallographic structures. Early reports have shown that the catalytic performance of MnO_x depends on the stoichiometric composition and follows the sequence of $\text{Mn}_3\text{O}_8 < \text{Mn}_3\text{O}_4 < \text{Mn}_2\text{O}_3 < \text{MnOOH}$,^{18,26} and the activity of MnO_2 materials strongly depends on their crystallographic phases of MnO_2 .^{30,31}

The physical and chemical properties of MnO_x nanostructures are found to be highly influenced by their chemical composition, crystallographic structure, as well as particle size and shape.^{12,13,32–36} In a recent work, Meng et al. demonstrated the structure–property relationship of various MnO_2 nanostructures toward bifunctional application of oxygen electrode in alkaline medium. They also found that OER and ORR activity greatly depends on their crystallographic nature and $\alpha\text{-MnO}_2\text{-SF}$ catalyst outperformed all other materials used in their study.³⁷ Therefore, with a view of promoting the wide-range applications of MnO_x in ORR necessitates a systematic study on the influential parameters such as nanoshapes with specific crystallography. The aim of this study is to comparatively investigate the catalytic properties of MnO_2 materials of a specific phase (α -crystallography) but with different morphologies in order to understand the influence of shape/geometry on resultant ORR activity and mechanism.

2. EXPERIMENTAL SECTION

2.1. Materials Used. KMnO_4 , $\text{MnSO}_4\cdot\text{H}_2\text{O}$, HCl (37%), and KOH (Merck); H_2SO_4 (98.08%) (Fisher Scientific); ethanol (99.9%) (Hayman); and Mn_2O_3 and Nafion solution (Sigma-Aldrich) were used here as analytical grade without any further purification. Milli-Q water was used for both synthesis of MnO_2 and electrochemical studies.

2.2. Preparation of MnO_2 Materials. We employed a hydrothermal method to prepare different shapes of MnO_2 material except for bulk MnO_2 . In a typical synthesis of $\alpha\text{-MnO}_2$ nanowires (NWs), 30 mL of homogeneous mixture of aqueous solutions containing 0.47 g of KMnO_4 and 0.50 g of $\text{MnSO}_4\cdot\text{H}_2\text{O}$ was transferred into a 50 mL Teflon-lined stainless steel autoclave and maintained at 140 °C for 24 h. The product was filtered, washed with distilled water and ethanol and then dried at 60 °C overnight.³⁸ A similar synthesis procedure was followed for the preparation of $\alpha\text{-MnO}_2$ nanorods (NRs) by using 0.394 g of KMnO_4 and 0.17 g of $\text{MnSO}_4\cdot\text{H}_2\text{O}$ in 35 mL at 180 °C for 16 h.³⁸

To prepare $\alpha\text{-MnO}_2$ nanotubes (NTs), 0.45 g of KMnO_4 and 1 mL of HCl (37%) were treated hydrothermally in 40 mL at 140 °C for 12 h.³¹ In the case of the $\alpha\text{-MnO}_2$ nanoparticle (NPs), 0.3 g of KMnO_4 and 0.2 mL of H_2SO_4 were treated in 25 mL at 150 °C for 4 h.³⁹ Layered potassium manganese oxide hydrate [$\text{K}_{0.27}\text{MnO}_2(\text{H}_2\text{O})_{0.54}$] [i.e., MnO_2 -nano flowers (NFs)] was prepared by hydrothermally using 200 mg of

KMnO_4 in 30 mL at 150 °C for 72 h.⁴⁰ Bulk $\alpha\text{-MnO}_2$ was prepared in a two-step procedure, initially 5 g of Mn_2O_3 refluxed in 50 mL of 6 M H_2SO_4 at 105 °C for about 12 h then the product was heat-treated at 250 °C with a flow of Ar gas in a quartz tubular furnace for 8 h.⁴¹

2.3. Characterization of MnO_2 Materials. The crystalline nature of the different MnO_2 materials were examined by powder X-ray diffraction (XRD) measurements using a PAN Analytical X'Pert PRO model X-ray Diffractometer with Cu $\text{K}\alpha$ radiation ($\lambda = 1.5418 \text{ \AA}$) from 10° to 80° at 0.02° step and a count time of 0.2 s. Thermogravimetric analysis (TGA) of the MnO_2 materials were carried out using TGA/DTA Instruments (model SDT Q 600) from room temperature to 800 °C at a heating rate of 10 °C min⁻¹ in air. Fourier transform-infrared (FT-IR) measurements were carried out by the KBr method using a Bruker Optic (GmbH, Germany) TENSOR 27 FT-IR spectrometer. FT-IR spectra were recorded in the transmittance mode over the range of 400–4000 cm⁻¹ by averaging 64 scans at a resolution of 4 cm⁻¹. Raman spectra were recorded with a Renishaw Invia Micro-Raman RM 1000 (Renishaw UK) system using a laser excitation wavelength of 532 nm (Nd:YAG), 0.5–1 mW, with a 1 μm focus spot in order to avoid photodecomposition of the samples. N_2 sorption isotherm for determining BET surface area and BJH pore size distribution was measured (Quantachrome Instruments NOVA 4000e) at 77 K.

The chemical composition of the prepared samples were analyzed by employing a BRUKER, (VEGA3, TESCAN, Germany) Scanning Electron Microscope equipped with EDX analysis. The morphology and surface nature of the MnO_2 materials were characterized by field-emission scanning electron microscopy (FE-SEM) using a Carl Zeiss AG Supra 55VP with an acceleration voltage of 5–30 kV. The particle size and dispersion of MnO_2 were examined using a transmission electron microscope (TEM, Tecnai G² 20) working at an accelerating voltage of 200 kV. ESR spectra of the MnO_2 materials were recorded using a Bruker EMX Plus spectrometer. The conditions for the measurement were X band: 100 kHz modulation with 6.0 G application; microwave power, 5 mW; central magnetic field, 3480 G; scan width, 200 G. All experiments were carried out at a liquid nitrogen temperature of 77 ± 1 K. X-ray photoelectron spectroscopy (XPS) analysis of the MnO_2 sample was performed using the Multilab 2000 (Thermoscientific, UK) photoelectron spectrometer fitted with a twin anode X-ray source. The Mn 2p core-level photoemission spectra were recorded using the Mg $\text{K}\alpha$ (1253.6 eV) source. Experimental data were curve fitted with a Gaussian and Lorentzian mix-product function after subtracting Shirley Background.

The XAFS measurements of Mn K-edge were performed in transmission mode at the Scanning EXAFS Beamline (BL-9) at the INDUS-2 Synchrotron Source, Raja Ramanna Centre for Advanced Technology (RRCAT), Indore, India. A Si(111) double-crystal monochromator (DCM) was used to obtain a monochromatic beam. A 1.5 m horizontal premirror with meridional cylindrical curvature used to obtain a collimate beam on the first crystal of DCM and rejection of higher harmonics of the beam. The second crystal of the DCM is a sagittal (bent in the direction perpendicular to the beam) cylinder with radius of curvature in the range of 1.28–12.91 m, which provides horizontal focusing to the beam. For XAFS measurement in the transmission mode, the sample was placed in between two ionization chambers to collect total incident

flux (I_0) before the sample in the first ionization chamber and transmitted intensity (I_t) after the sample in the second ionization chamber. The energy range of XAFS was calibrated using standard Mn metal foil at 6539 eV. The set of EXAFS data has been analyzed using FEFF 6.0 code.⁴² This includes background reduction and Fourier transform to derive the $\chi(R)$ versus R spectra from the absorption spectra (using ATHENA software),⁴³ generation of the theoretical EXAFS spectra starting from an assumed crystallographic structure, and finally fitting of experimental data with the theoretical spectra using ARTEMIS.⁴³

2.4. DFT Method. The catalytic activity of $\alpha\text{-MnO}_2 \cdot 0.25\text{H}_2\text{O}$ toward oxygen reduction was studied within the framework of first-principles density functional theory (DFT) calculations, using Vienna Ab-initio Simulation Package (VASP).⁴⁴ Projected augmented wave (PAW) pseudopotentials were used to represent the potentials of the atoms involved.⁴⁵ The exchange-correlation energy was corrected by the usage of Generalized Gradient Approximations including the onsite coulombic interaction (GGA+U).⁴⁶ The values of 4.5 and 0.75 eV were used for the onsite columbic interaction (U) and exchange energy (J) terms respectively, which were adopted from ref 47. The self-consistent calculations were repetitively performed until the forces on each ion and the total energy converge below 0.01 eV/Å and 10^{-5} eV, respectively. The surfaces (110), (200), (211), and (310) of $\alpha\text{-MnO}_2 \cdot 0.25\text{H}_2\text{O}$ are constructed with the vacuum thickness of at least 10 Å to avoid the interaction of the atoms of surface slabs from its periodic image. Throughout our calculations, the spin polarized calculations were carried out, in which, the spin moments of Mn atoms were aligned ferromagnetically.

2.5. Electrochemical Methods. Oxygen reduction experiments were carried out by using a rotating ring disc electrode (ALS, model RRDE 3A) technique throughout by employing an Ivium model bipotentostat (BiStat). Oxygen reduction studies were carried out by employing a glassy carbon (GC) disc electrode of 4 mm dia (geometric area = 0.1257 cm^2) and Pt ring electrode. The GC electrode surface was firmly polished with alumina suspensions (particle size 1, 0.3, and $0.05 \mu\text{m}$, respectively). Then the tip was cleaned ultrasonically for several minutes with pure ethanol and distilled water to remove the traces of contamination. Four microliters of the slurry (to achieve 0.14 mg cm^{-2} loading mass) in Nafion (0.5%) solution was drop-casted on the bare GC electrode. The ORR performance was investigated by linear sweep voltammetry (LSV) under constant O_2 gas flow, with a sweep rate value 5 mV s^{-1} in 0.1 M KOH solution with Pt foil as a counter electrode and saturated calomel as a reference electrode.

3. RESULTS AND DISCUSSIONS

3.1. Physical, Structural, and Morphological Characterization. The phase purity and crystal structure of the MnO_2 materials have been examined by XRD. Figure 1A represents the XRD patterns of the hydrothermally prepared MnO_2 nanomaterials as given in the figure. From the XRD patterns, all the reflections except nanoflowers can be indexed to the body-centered tetragonal $\alpha\text{-MnO}_2$ (JCPDS no. 44-0141, space group $14/m$, $a = b = 9.784 \text{ \AA}$, $c = 2.863 \text{ \AA}$), indicating the appreciable phase-purity of the obtained $\alpha\text{-MnO}_2$ materials and no other impurities are observed.⁴⁷ $\alpha\text{-MnO}_2$ phase has a tunnel structure parallel to the c axis. The tunnel cavity is as large as 0.46 nm , which is the foremost reason to use $\alpha\text{-MnO}_2$ as molecular/ion sieves. In connection to this, few large cations

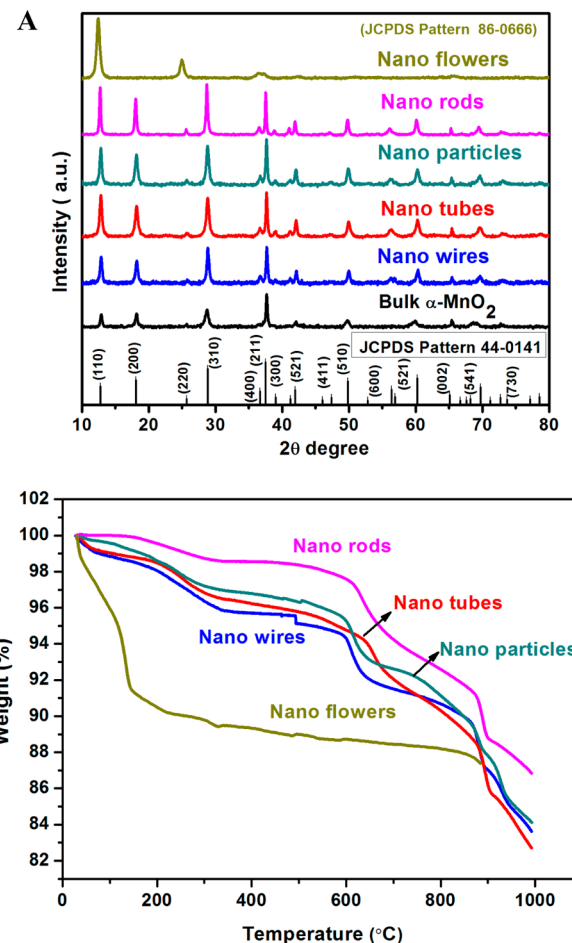


Figure 1. (A) X-ray diffraction patterns of bulk $\alpha\text{-MnO}_2$ and different shapes of MnO_2 prepared in this work along with their JCPDS patterns. (B) Thermogravimetric analysis of five different MnO_2 nanoshapes recorded in air at a heating rate of $2 \text{ }^\circ\text{C min}^{-1}$.

and water molecules could also be intercalated into the tunnel cavity from the starting materials during the hydrothermal process. The nanoflower morphology is potassium manganese oxide hydrate [$\text{K}_{0.27}\text{MnO}_2(\text{H}_2\text{O})_{0.54}$], a layered material and its XRD pattern matches well with the JCPDS 86-0666 file. The chemically adsorbed water could be detected by thermogravimetric analysis (TGA). Figure 1B shows the TGA graphs of as synthesized materials in air. It shows a weight loss of $\sim 18\%$ after being heated to $1000 \text{ }^\circ\text{C}$. The TGA profile and the range of weight loss are very similar to those reported for hydrothermally synthesized layered MnO_2 nanobelts.⁴⁹ There are three apparent weight-loss stages corresponding to (i) loss of water, $\sim 5\%$ (room temperature to $300 \text{ }^\circ\text{C}$), (ii) $\text{MnO}_2 \rightarrow 1/2 \text{Mn}_2\text{O}_3$, 4% ($600 \text{ }^\circ\text{C}$), and (iii) $1/2 \text{Mn}_2\text{O}_3 \rightarrow 1/3 \text{Mn}_3\text{O}_4$, 7% ($940 \text{ }^\circ\text{C}$). The final product after the TG treatment up to $1000 \text{ }^\circ\text{C}$ is Mn_3O_4 .⁴⁹ The desorption of physisorbed and/or chemisorbed water molecules from MnO_2 materials are greatly influenced by the shape of the material as seen in Figure 1B. For example, in the case of $\alpha\text{-MnO}_2$ nanotubes, it requires at least $150\text{--}200 \text{ }^\circ\text{C}$ higher temperature for the water molecules to be pushed out of the tubular-voids structure when compared to nanoflower shape. $\alpha\text{-MnO}_2$ nanotubes retains the structural water molecules by offering a stronger interaction, whereas in the case of nanoflower morphology, the open platelet structure (in the following section) could pave a way to lose the water

Table 1. Obtained BET, EDXA, XPS, and ESR Structural Parameters for Various MnO_2 Materials Studied in This Work

sample	BET surface area (m^2/g)	pore volume (cc/g)	pore diameter (nm)	Mn atomic %	K atomic %	atomic ratio Mn/K	XPS $\Delta 2\text{p}$ value (eV)	<i>g</i> -value from ESR
nanowires	27.7	0.094	3.62	35.85	3.58	10.01	11.67	2.01
nanotubes	21.1	0.086	4.05	26.02	3.18	8.18	11.78	2.01
nanoparticles	34.7	0.129	3.26	33.38	3.50	9.54	11.39	2.04
nanorods	24.8	0.063	3.28	31.42	3.11	10.10	11.61	2.04
nanoflowers	32.4	0.173	4.07	27.85	6.49	4.29	11.64	2.14

molecules at lower temperatures. The obtained Mn/K atomic ratio of $\sim 10\%$ for the four $\alpha\text{-MnO}_2$ shapes except nanoflowers (Table 1) corroborates the tunnel structure explained in XRD studies. However, a low value of 4.3% in the case of nanoflowers testifies its layered structure where it contains more potassium ion content. The BET specific surface areas were measured by nitrogen adsorption isotherms at 77 K (as shown in the Supporting Information), and their values are included in Table 1. $\alpha\text{-MnO}_2$ nanoparticles possess the highest BET surface area value of $34.7 \text{ m}^2 \text{ g}^{-1}$ among various morphologies prepared in this work.

In Figure 2, the first row images (A, D, G, J, M) show the FE-SEM morphology of five different MnO_2 shapes prepared in this work. The MnO_2 materials obtained are appreciably homogeneous in their respective shapes. The nanowire morphology grown into few micrometer length wire with an $\sim 20 \text{ nm}$ diameter. Similarly, nanotubes composed with a wall thickness of $\sim 25 \text{ nm}$ along with 20 nm inner tube diameter are shown clearly. FE-SEM picture of nanoparticle morphology (Figure 2G) contains uniform particle distribution with size 50 to 80 nm range. In order to examine their detailed structure, we have performed TEM analysis of all the MnO_2 samples and results are presented in Figure 2 (B, E, H, K, and N). The individual nanoshapes are shown in their respective micrographs. Nanorod and nanoflower morphologies are clearly seen in their respective TEM images. In addition to this, the lattice parameters calculated from the high-resolution pictures, namely, 0.37 nm (nanowires), 0.68 nm (nanotubes), and 0.23 nm (nanoparticles) are in very good agreement with their corresponding lattice parameters calculated from XRD peaks. These TEM and selected area electron diffraction (SAED) investigations indicate the high-quality single-crystalline nature of the obtained MnO_2 nanomaterials.

Fourier transform-infrared (FT-IR) and Raman scattering (RS) spectroscopy have been proved to be useful alternatives and/or supplements to X-ray diffraction for structural characterizations of materials. It is based on the fact that they are sensitive to crystalline disorders as well as different local structural properties. FT-IR and RS spectroscopy can yield more complete and reliable description of materials and further confirmation of our samples. FT-IR spectra of the samples are given in Figure 3A; IR spectra of nanoflowers and nanoparticles exhibit a relatively strong band around $\sim 3430 \text{ cm}^{-1}$, which is caused by the adsorbed interlayer hydrates. The bands in the region between 400 and 800 cm^{-1} could be assigned to Mn–O lattice vibration samples.^{50,51} Figure 3B represents the Raman spectra of MnO_2 nanomaterials of different shapes prepared in this work. All the MnO_2 materials showed two diagnostic RS bands at the high frequency region, 574.2 and 641.8 cm^{-1} , belonging to A_g spectroscopic species that originate from breathing vibrations of MnO_6 octahedra within a tetragonal hollandite-type framework.^{52,53} It is emphasized that the relative intensities of two high-frequency Raman bands at 570

and 635 cm^{-1} are correlated to the nature of the tunnel species.⁵² Hence, the spectrum reflects the good crystallinity of the MnO_2 materials, which is in agreement with the other structural studies reported above.

3.2. X-ray Photoelectron Spectroscopy and Electron Paramagnetic Resonance Studies. The surface chemistry and oxidation states of the MnO_2 materials were examined by using the XPS technique. Figure 4 shows the comparison of core-level XPS signal corresponds to Mn 2p in all the MnO_2 materials prepared in this work. The figure reveals that the Mn 2p_{3/2} and 2p_{1/2} centered at 642.0 and 653.9 eV, respectively, which indicates the predominant oxidation state of Mn atoms in MnO_2 are +4. The difference between peak positions of Mn 2p_{3/2} and 2p_{1/2} for all the MnO_2 nanomaterials are included in Table 1. Agreement among the above studies is reasonable with an average binding energy of 642.3 and 654 eV.^{54–56} The O(1s) spectrum (Figure 5, panels A, B, C, D, and E) has a maximum near 530 eV, with a pronounced tail on the high-energy side. There are at least three contributions that could be identified in the spectrum. Idealized manganite composition requires equal abundance of oxide (O^{2-}) and hydroxide (OH^-), hence equal contributions of these species to the O(1s) spectrum. The high-energy tail may include physisorbed, chemisorbed, and structural H_2O and water in poor electrical contact with the mineral surface.⁵⁷ The fit to the O(1s) spectrum is reasonable (Figure 5) and demonstrates that O^{2-} and OH^- are the dominant states. However, the nanowire and nanorod morphologies possess high intensity of the O^{2-} peak rather than the OH^- peak may be due to the abundance of the oxide state which contributes to the formation of the network. The binding energy of the H_2O peak is low (532.3 eV), suggesting that the water is largely chemisorbed or structurally bound.⁵⁷

The magnetic structure of the manganese oxide spinel is a result of competition between 90° direct $\text{Mn}^{4+}\text{--Mn}^{4+}$ antiferromagnetic and 90° super exchange $\text{Mn}^{4+}\text{--O}^{2-}\text{--Mn}^{4+}$ ferromagnetic interactions. Therefore, the spinels can be regarded as systems where antiferro- and ferromagnetic interactions act on an atomic Mn site.⁵⁸ Taking into account the thermal stability of the manganese oxide spinels, one may assume to localize the Mn^{4+} ions in low-symmetry crystal fields near oxygen defects. Completing this picture, one may say that Mn^{4+} and oxygen defects coagulate into complex associates, whose amount increases as the cooling rate increases.⁵⁹ Figure 6 shows the EPR spectra recorded for five different MnO_2 samples at liquid nitrogen temperature. In our case, the morphologies, namely, nanowire, nanotube, and nanoflower materials displayed a sharp and narrow signal, whereas the nanoparticles and nanorods produce a broad line with splitting characteristics. A similar narrow signal was observed for the $\text{Li}_4\text{Mn}_5\text{O}_{12}$ spinel (containing only Mn^{4+}) and was assigned to Mn^{4+} having its first metal coordination sphere 4Mn^{4+} and 2Li^+ ions.⁶⁰ Moreover in a recent report by Chen et al, it has been

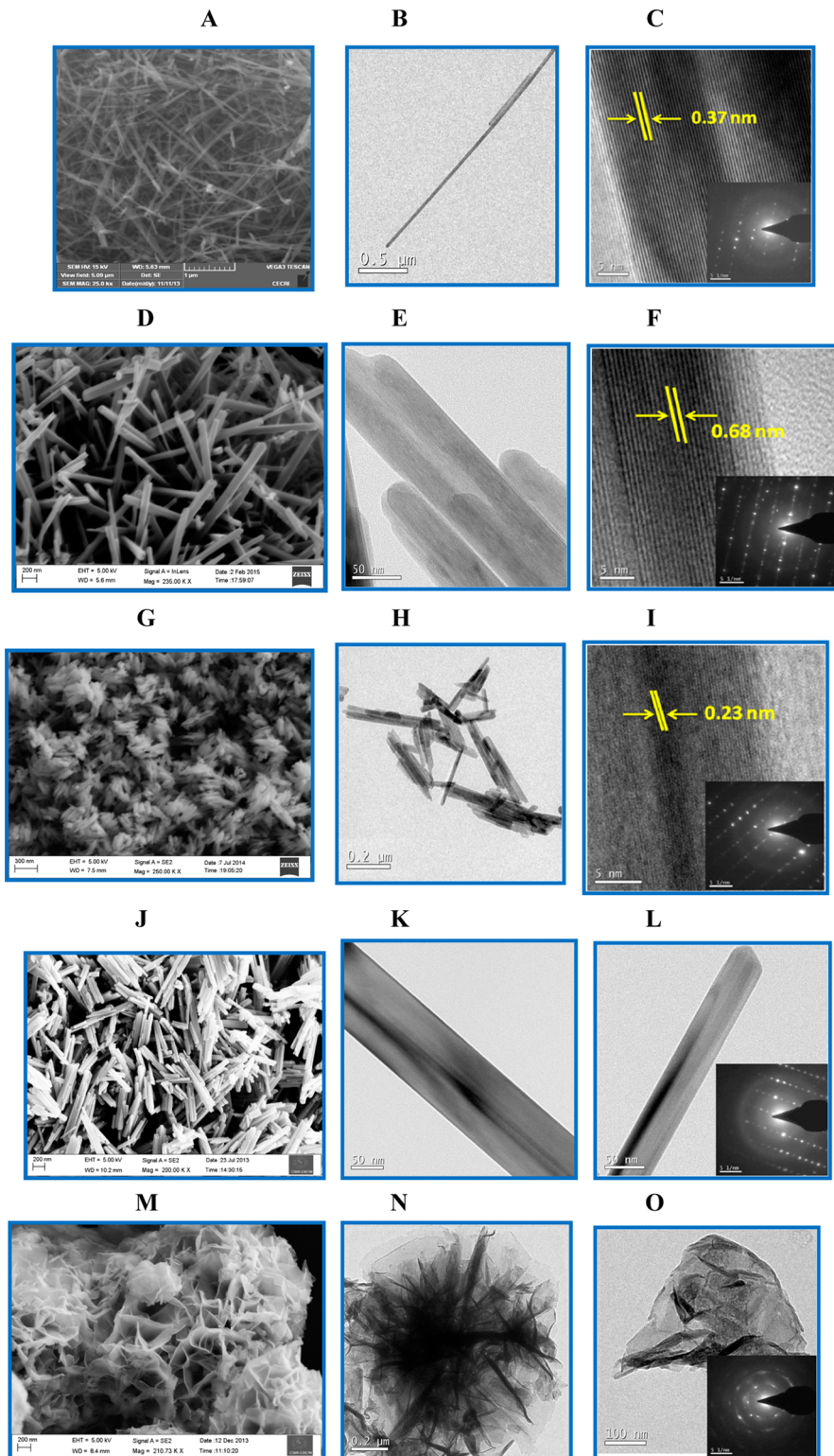


Figure 2. SEM morphologies recorded for nanowires, nanotubes, nanoparticles, nanorods, and nanoflowers (A, D, G, J, M), corresponding TEM images (B, E, H, K, N) of individual shapes and (C, F, I, L, O) lattice fringes, high resolution of magnified shape and SAED patterns, respectively.

explained in detail about the origin and occurrence of “wing” as well as hyperfine splitting lines in the case of MnO_2 materials that are highly sensitive to their nanogeometric grain size effects.⁶¹ The observed g-value for different morphology has been included in Table 1. It can be seen that the g-values are ~ 2.0 , which indicates that the oxidation state of Mn is +4.

3.3. X-Ray Absorption Spectroscopy Studies. Figure 7A shows Mn K-edge XANES spectra for Mn foil, Mn_2O_3 (Mn^{3+}), MnO_2 (Mn^{4+}) standards, and different MnO_2 shapes. The first inflection point of Mn edge has been measured for all different MnO_2 shapes and compared with Mn^{3+} and Mn^{4+} standards which confirm the valence state of Mn atoms in both bulk α - MnO_2 as well as in different shapes are found as 4+. Our

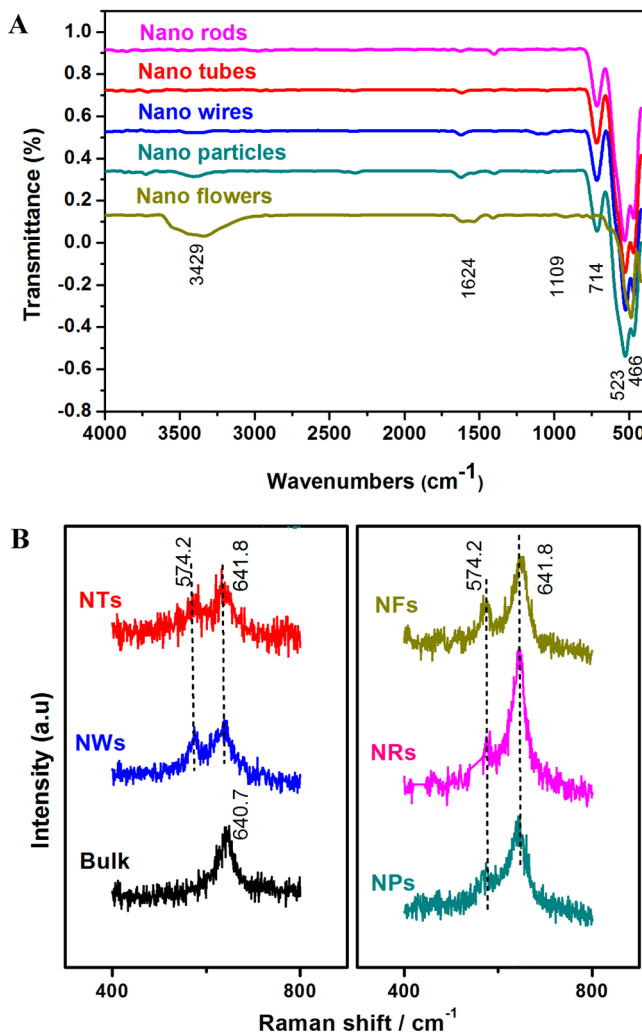


Figure 3. (A) FT-IR spectra and (B) Raman scattering spectra of different MnO_2 materials.

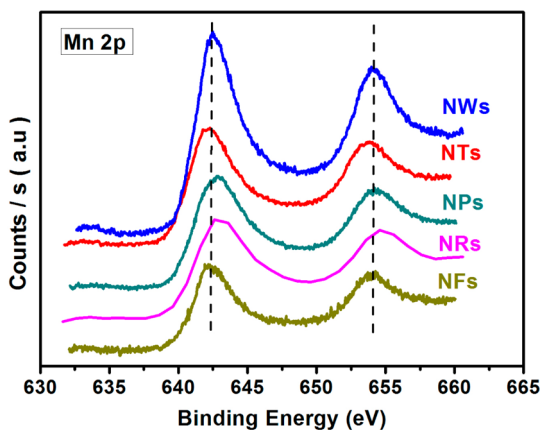


Figure 4. XPS spectra for the Mn-2p region of three different MnO_2 nanoshapes as mentioned in the figure.

observation and value are in good agreement with the recent X-ray absorption spectroscopic studies on manganese oxide octahedral molecular sieves reported by Suib et al.⁶² The inset of Figure 7A shows pre-edge spectra of MnO_2 and different shapes prepared in this work. The pre-edge peak is mainly attributed due to electric dipole forbidden transition corre-

sponding to the $1s \rightarrow 3d$ transition, which in this case is partially allowed because of the following phenomena: (i) electric quadrupole coupling s–d transition and (ii) p–d orbital hybridization. The inset of Figure 7A shows the pre-edge region of Mn K-edge; one may note that there are multiple peaks A and B which split to pre-edge peaks originating from the separation of degenerated 3d levels under the octahedral crystal field from $1s \rightarrow 3d$ (t_{2g}) and $1s \rightarrow 3d$ (e_g) transition, respectively, whereas the main absorption edge was attributed to the $1s \rightarrow 4p$ transition. The prepeak of bulk MnO_2 is less intense when compared to all other MnO_2 nanoshapes (NWs, NPs, NTs, NRs, and NFs) (see Figure S4 of the Support Information). Such an observation may cause from the more mixed p–d orbital hybridization facilitated in MnO_2 nanoshapes.

Figure 7B shows the Fourier transforms (FT) of the Mn K-edge $k^3\chi(k)$ spectra for bulk $\alpha\text{-MnO}_2$ and all other MnO_2 shapes. The observed FT spectra for bulk MnO_2 and nanoshapes (except nanoflower morphology) are similar due to their identical crystal structure. For fitting XAFS data, $\alpha\text{-MnO}_2$ crystalline $I4/m$ tetragonal structure has been used.⁶³ In the structure of $\alpha\text{-MnO}_2$, the Mn atoms occupy the Wyckoff position (0.34691, 0.16546, 0) and the O1 atom occupies the position with (0.15350, 0.19940, 0), O2 (0.53890, 0.15950, 0), and O3 (0, 0, 0.5) coordinates, where the Mn atom is surrounded by 4 O atoms at 1.885 Å, 2 O atoms at 1.947 Å, and by 4 Mn at 2.850 Å distances.

It is well-known that normally a slight distorted MnO_6 octahedron is usually present in $\alpha\text{-MnO}_2$ catalysts.⁶⁴ We have carried out a detailed XAFS fitting in order to obtain Mn–O and Mn–Mn actual distances in our MnO_2 nanoshapes. For Mn, the K-edge XAFS fitting distance of Mn–O and Mn–Mn as well as the Debye–Waller (DW) factor has been taken as a guess parameter. The best fit of XAFS parameters are listed in Table 2, containing coordination number N , bond distance R (Å), and the Debye–Waller factor σ^2 (\AA^2) of the Mn–O neighbor atom and Mn–Mn nearest-neighbor atoms. From fitting of XAFS, bulk $\alpha\text{-MnO}_2$ both distorted Mn–O and Mn–Mn distances are coming at lower values than theoretical distances. It has been observed that for $\alpha\text{-MnO}_2$ nanowires and nanoparticles, the Mn–O1 bond distance has been slightly elongated and, consequently, the Mn–O2 bond distance becomes shortened with respect to the bulk $\alpha\text{-MnO}_2$ values. In contrast to the above for other shapes, like, nanorods and nanoflowers, the Mn–O2 bond distance becomes elongated when compared to bulk $\alpha\text{-MnO}_2$. Moreover, it is interesting to note that in all the shapes except for the nanoflowers, the observed Mn–Mn distances are greater than bulk Mn–Mn distance of 2.819 Å as listed in Table 2.

3.4. Electrochemical Oxygen Reduction Studies on Different MnO_2 Shapes. To assess the shape-dependent electrocatalytic activity of different MnO_2 catalysts prepared in this work, rotating disc electrode (RDE) experiments were performed in the 0.1 M KOH electrolyte solution. Figure 8 shows the hydrodynamic linear sweep voltammogram (LSV) obtained for the $\alpha\text{-MnO}_2$ nanowire catalyst-coated film electrode recorded at 5 mV s⁻¹ in O₂-saturated 0.1 M KOH solution at different electrode rotation speed. The ORR, which started at −0.1 V (SCE) on the MnO_2 catalyst surface gradually passed through a mixed control between −0.15 and −0.45 V and attained complete mass-transfer control at potentials less than −0.5 V. The expected increase in the diffusion limited current in the disk measurement was observed as a function of

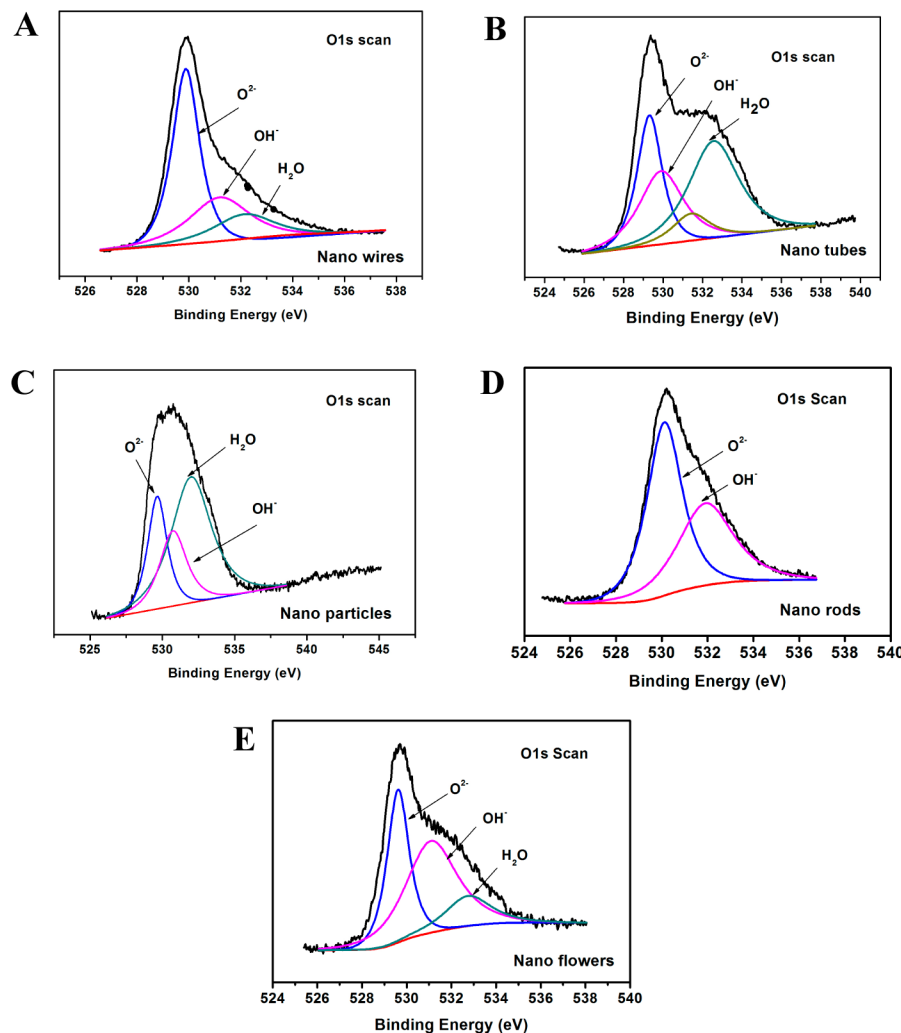


Figure 5. XPS spectra for the O 1s region of five different MnO_2 as mentioned in the figure.

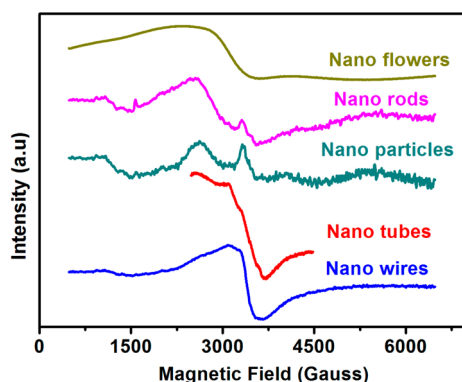


Figure 6. EPR spectra of five different MnO_2 nanoshapes recorded in liquid nitrogen temperature.

rotation speed. The Koutecky–Levich plots drawn at different potentials showed a linear dependence at all potentials (Figure 9, panels A and B). The linear and the parallel form of these plots usually indicate first-order kinetics with respect to molecular oxygen, although this criterion is not very specific.⁶⁵ The overall current (i) in the reaction measured at RDE was the result of contributions from the kinetic current (i_k), diffusion limiting current in the Nafion film covered catalyst layer (i_f), and diffusion limiting current through the solution

boundary layer (i_d). According to the Koutecky–Levich (eq 1), the overall current

$$\frac{1}{i} = \left(\frac{i}{i_k} \right) + \left(\frac{1}{i_f} \right) + \left(\frac{1}{i_d} \right) \quad (1)$$

Since the amount of Nafion in the electrode is small, and the film resistance is sufficiently small ($\sim 0.01 \text{ cm}^2/\text{mA}$), the overall current can be described as

$$\frac{1}{i} = \left(\frac{i}{i_k} \right) + \left(\frac{1}{i_d} \right) \quad (2)$$

The value for i_d can be represented as

$$i_d = 0.62nFACD^{2/3}\nu^{-1/6}\omega^{1/2} \quad (3)$$

where n is the number of electrons transferred in the reaction, F is the Faraday constant, A is the geometric surface area of the electrode, C the concentration of oxygen in the solution at atmospheric pressure, and D the diffusion coefficient of oxygen, ν is the kinematic viscosity of the electrolyte ($0.01 \text{ cm}^2 \text{ s}^{-1}$), and ω is the angular velocity (rad s^{-1}).

Results were also obtained for all other MnO_2 shapes prepared in this work, and the disc/ring response obtained by rotating ring-disc electrode configuration are compared in Figure 10A. These results clearly show that the onset potential of ORR and the amount of peroxide produced at MnO_2 surfaces strongly depended on the shape of the MnO_2 material. For example, the $\alpha\text{-MnO}_2$ nanowire catalyst displayed $\sim 100-$

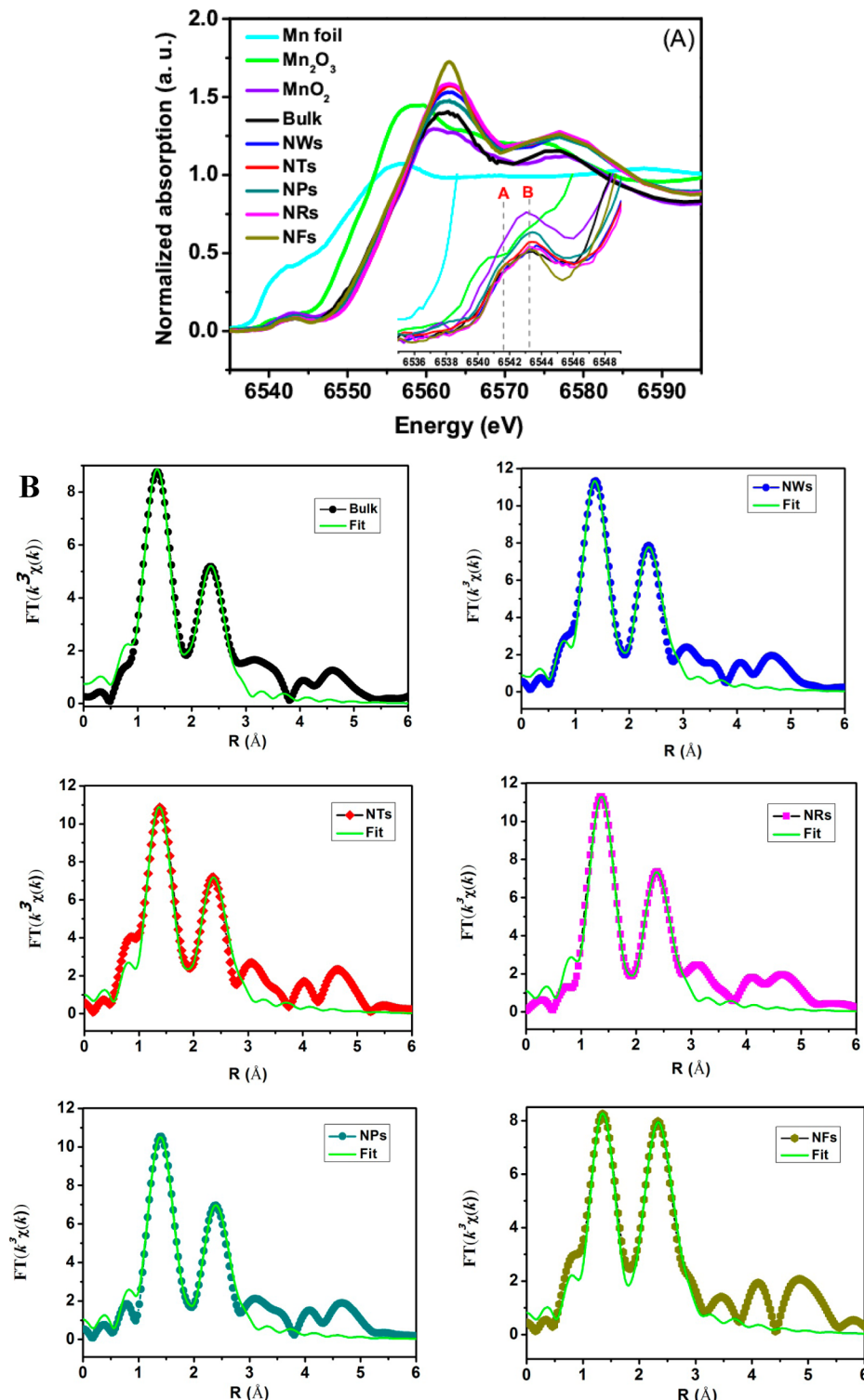


Figure 7. (A) Normalized XANES spectra at Mn K-edge for Mn foil, Mn₂O₃ (standard), MnO₂ (standard), and different MnO₂ nanoshapes. The inset shows a pre-edge feature for all MnO₂ samples. (B) Fourier transform of k^3 -weighted of Mn K-edge XAFS for different MnO₂ nanoshapes.

150 mV lower in $E_{1/2}$ value toward ORR when compared to nanoparticle and nanoflower catalysts under identical experimental conditions. Since negligible amounts of peroxide were detected at the ring electrode in the kinetic region, on the basis of these measurements, it is impossible to conclude whether the reaction involved a four-electron reduction in a direct or series pathway.⁶⁵ Figure 10B shows the Koutecky–Levich plots drawn at -0.8 V for five different MnO₂ surfaces. It is clear that

the slopes of these lines significantly vary with the shape of the MnO₂ catalyst, and moreover, by substituting values like C , the concentration of oxygen in solution at atmospheric pressure is (1.14×10^{-6} mol cm⁻³), and D , the diffusion coefficient of oxygen (1.73×10^{-5} cm² s⁻¹) in eq 3, yields the constant B value which in turn yields the “ n ” value (i.e., the number of electrons transferred during oxygen reduction reaction). It can be seen from Table 3 that in the case of the α -MnO₂ nanowires

Table 2. Observed Mn K-edge XAFS Fitted Mn–O Bond Distance Mn–Mn Distance in Angstroms and Debye–Waller (DW) Factor for Various MnO_2 Materials

sample	path	co-ordination number (N)	theoretical distance R (\AA)	fitted distance R (\AA)	Debye–Waller factor σ^2 (10^{-3}\AA^2)
bulk $\alpha\text{-MnO}_2$	Mn–O1	4	1.885	1.847(6)	0.004(1)
	Mn–O2	2	1.947	1.909(7)	0.004(1)
	Mn–Mn	4	2.850	2.819(8)	0.011(2)
MnO_2 nanowires	Mn–O1	4	1.885	1.857(7)	0.003(1)
	Mn–O2	2	1.947	1.884(3)	0.003(3)
	Mn–Mn	4	2.850	2.824(9)	0.008(1)
MnO_2 nanoparticles	Mn–O1	4	1.885	1.892(7)	0.003(1)
	Mn–O2	2	1.947	1.877(2)	0.003(2)
	Mn–Mn	4	2.850	2.847(9)	0.008(2)
MnO_2 nanotubes	Mn–O1	4	1.885	1.864(6)	0.003(1)
	Mn–O2	2	1.947	1.909(3)	0.003(2)
	Mn–Mn	4	2.850	2.826(8)	0.008(2)
MnO_2 nanorods	Mn–O1	4	1.885	1.859(3)	0.003(1)
	Mn–O2	2	1.947	1.931(3)	0.003(2)
	Mn–Mn	4	2.850	2.839(5)	0.008(2)
MnO_2 nanoflowers	Mn–O1	4	1.885	1.868(3)	0.004(1)
	Mn–O2	2	1.947	1.919(3)	0.004(2)
	Mn–Mn	4	2.850	2.818(6)	0.007(2)

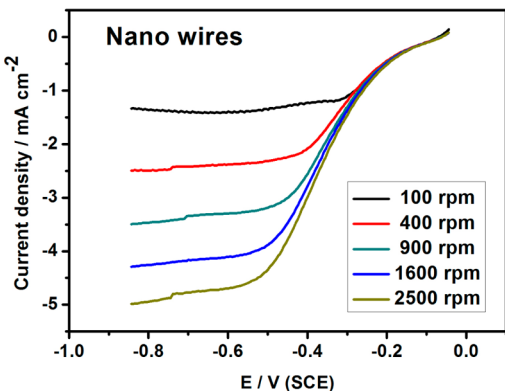


Figure 8. Electrochemical oxygen reduction reaction recorded with a catalyst loading of 0.14 mg cm^{-2} of $\alpha\text{-MnO}_2$ nanowires on a glassy carbon electrode at a scan rate of 5 mV sec^{-1} in 0.1 M KOH solution with different electrode rotation rates as mentioned in the figure.

catalyst, the observed n value is 3.5, and the value is very close to a complete four-electron reduction of molecular oxygen to water. In contrast to this, the observed n -value for MnO_2 nanoflower catalyst is 1.9 and for $\alpha\text{-MnO}_2$ nanoparticle, it is 2.3. In both cases, the observed n -value is close to 2, which testifies that flower and particle shapes favors a 2-electron reduction process of molecular oxygen into hydrogen peroxide. It is worth mentioning here that studies concerning dependence of reaction pathway or mechanism of ORR with respect to MnO_2 shapes/geometry have not been reported yet.

The electrochemical oxygen reduction is known to proceed either in a four-electron step to H_2O or in a two-electron step to H_2O_2 . In general, the four-electron step is considered the major reaction pathway on polycrystalline platinum and carbon support Pt/C catalysts,^{66,67} whereas the two-electron step predominantly occurs in the case of non-Pt-based catalysts.⁶⁸ The reaction pathway of the ORR which is a measure of the formation rates of H_2O and H_2O_2 can be determined quantitatively with an RRDE measurement. Such measurement was carried out by setting the potential of the ring electrode at 0.316 V (SCE), where the complete oxidation of H_2O_2 formed by oxygen reduction on the disc electrode was under a

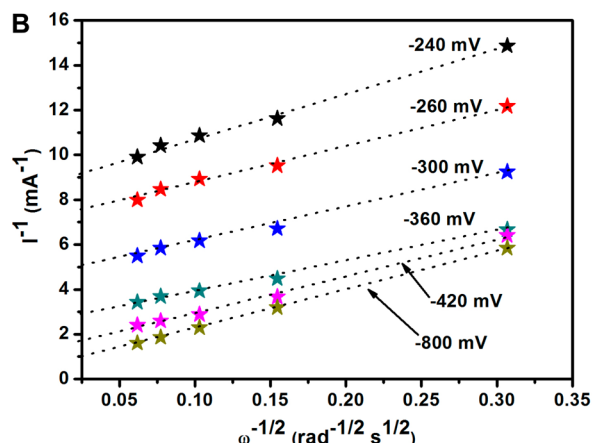
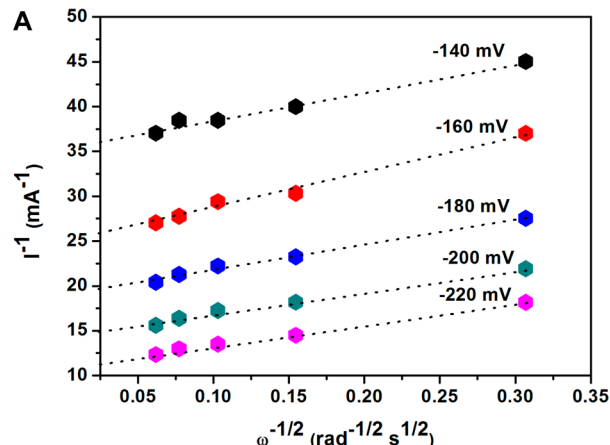


Figure 9. Koutecky–Levich plots recorded at different potentials for the data obtained from Figure 8.

diffusion-controlled process.⁶⁸ The percentages of the current associated with peroxide generation at -0.8 V was calculated using eq 4 for all of the MnO_2 catalysts employed in this work.

$$\% \text{H}_2\text{O}_2 = 2(I_R/N)/I_D + (I_R/N) \quad (4)$$

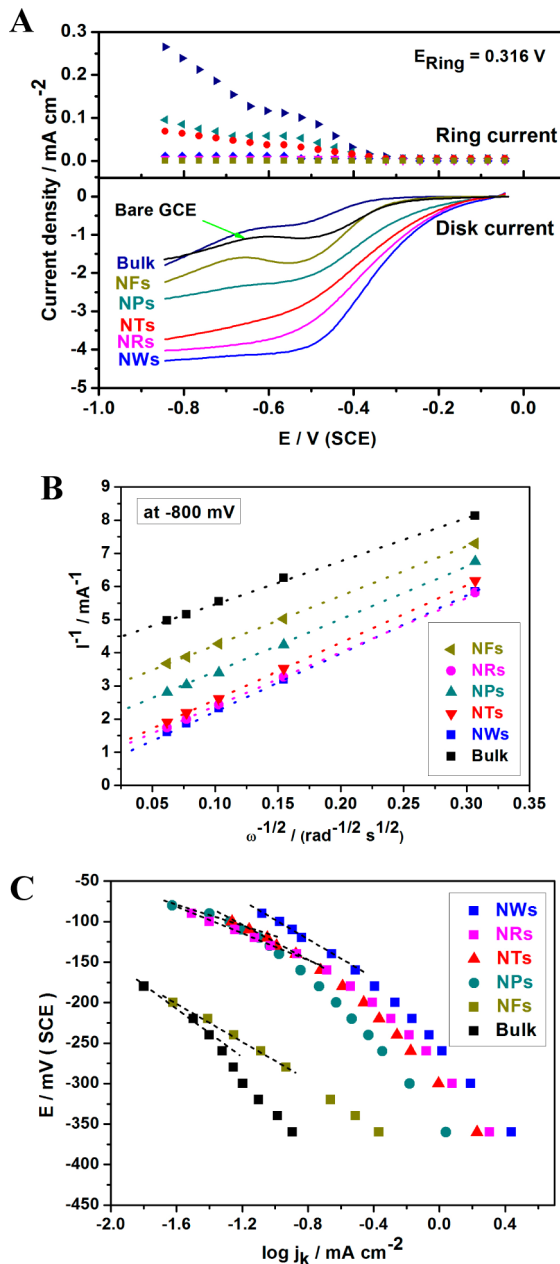


Figure 10. (A) Comparison of rotating ring disc electrode responses of five different MnO_2 nanoshapes with a catalyst loading of 0.14 mg cm^{-2} on a glassy carbon electrode at a scan rate of 5 mV sec^{-1} in 0.1 M KOH solution with 1600 rpm electrode rotation rate as mentioned in the figure. The ring potential was maintained constant at 0.316 V (SCE). (B) Comparison of Koutecky-Levich plots for five different MnO_2 nanoshapes recorded at -0.8 V (SCE) as mentioned in the figure. (C) Comparison of Tafel plots for electrochemical oxygen reduction reaction for five different MnO_2 nanoshapes as mentioned in the figure.

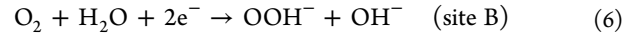
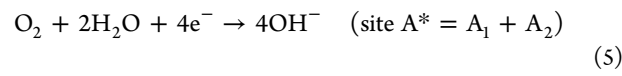
where I_D is disc current, I_R is ring current, and N is the collection efficiency coefficient which is 20%. Table 3 includes the amount of hydrogen peroxide produced for all the MnO_2 catalysts studied in this work. It is interesting to note that $\alpha\text{-MnO}_2$ nanorods produce the least amount of $\sim 2\%$, and $\alpha\text{-MnO}_2$ nanowires produced $\sim 4\%$ peroxide during ORR, which in turn supported their observed n -values which are close to 4. On the other hand, for example $\alpha\text{-MnO}_2$ nanoparticles produces $\sim 40\%$ and MnO_2 nanoflowers produced $\sim 24\%$

Table 3. Obtained ORR Kinetic Parameter, Calculated n -Value and % of Hydrogen Peroxide Produced during Reaction for Various MnO_2 Shapes

sample	Tafel slope value (mV/decade)	n -Value from KL plot at -0.8 V (SCE)	% of H_2O_2 produced at -0.8 V (SCE)
nanowires	65	3.5	3.66
nanotubes	90	3.0	21.44
nanoparticles	90	2.3	39.50
nanorods	65	3.2	1.97
nanoflowers	115	1.9	23.89
bulk- MnO_2	120	1.6	106.38

peroxide product, which is strongly supported by their observed n -value close to 2.

The observed differences in the n values, which seem more influenced by the nanoshape-geometry MnO_2 materials could be possibly explained as follows. The overall 4-electron ORR in alkaline medium is shown in eq 5. This can be achieved by a direct pathway or a series pathway involving a peroxide intermediate.⁶⁹ The direct pathway proceeds through a sequence of steps such that all four electron transfers of (eq 5) occur on the same catalytic site. In the series pathway, there is an initial 2-electron reduction of oxygen to peroxide (eq 6), likely proceeding in two distinct electron-transfer steps (not shown), followed by either one of two possibilities: via a 2-electron reduction step of peroxide to water (eq 7) or the peroxide disproportionation reaction (eq 8) that produces reactant O_2 gas in half of the original quantity via a chemical and not electrochemical step. This $1/2\text{O}_2$ is subsequently reduced back to peroxide with (eq 6) and (eq 7) cycled repeatedly until reaching a theoretical limit of an overall 4-electron process.⁶⁹ In the series pathway, it is plausible that two completely different catalytic sites can participate in the reactions (eq 5, eq 7, and eq 8).



While the subject of ORR mechanisms on MnO_2 -based catalysts is still being explored, several research groups have proposed a series pathway consisting of reactions 6 and 7 as the likely mechanism.⁷⁰ In this particular pathway, reaction 6 has been shown to occur either on the electrode (Supporting Information) onto which MnO_2 is deposited, such as carbon or gold or on $\text{Mn}^{(\text{IV})}/\text{Mn}^{(\text{III})}$ sites of MnO_2 , while the catalytic activity for reaction 8 has been attributed to MnO_2 .^{69,26} In conclusion, it can be postulated that both $\alpha\text{-MnO}_2$ nanowires and $\alpha\text{-MnO}_2$ nanorods are capable of executing reaction 5 on a single catalytic site due to its nanogeometry effect (i.e., complete four electron reduction on a single active site). On the other hand, $\alpha\text{-MnO}_2$ nanoparticle and MnO_2 nanoflower surfaces encourages the reaction 6 to occur on one active site and reactions 7 and 8 on another site⁶⁹ (i.e., only feasible to execute two electron reduction on a single active site), which reflected through their lower n values observed in our study.

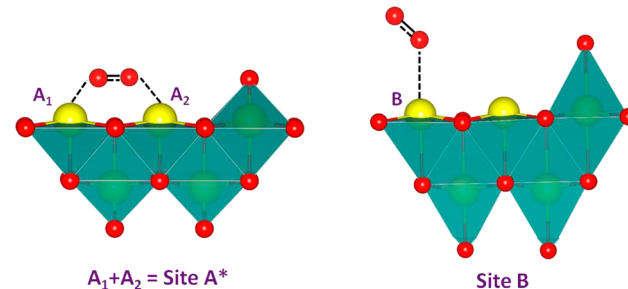
This aspect can be better visualized by recalling that the mechanism followed by the ORR depends on the type of

interaction between the oxygen molecules with the catalyst surface.⁷⁰ It is well-documented that the oxygen molecules adsorb in a horizontal (respect to O=O bond) mode on manganese oxide surfaces (site A*), which proceed through a bridge-type configuration.⁷¹ Bridge-type interactions conduct to the dissociation of O₂, which is consistent with the direct 4-electron reduction pathway. On the other hand, ORR with a 2-electron reduction pathway can be satisfactorily explained only if the interaction of O₂ with the catalyst surface through the end-on or vertical mode of adsorption (site B) (Pauling model) is assumed. The structure of these compounds is formed by different geometric arrangements of edge-sharing MnO₆ octahedra, resulting in several crystallographic orientations.

In the previous literature, it is proposed that a common feature of MnO₂ polymorphs is the presence of structural defects which influence several properties of these materials such as the electrochemical activity, induced photoconductivity,⁷² etc. A cation-vacancy model has been proposed by Ruetschi⁷³ to explain how the presence of these structural defects affects some of these properties. The model assumes that the oxygen sublattice is complete and that vacancies occur only on the manganese sublattice. The cation defects are manifested as a change of the oxidation state from Mn⁴⁺ to Mn³⁺ and as a manganese cation vacancy. It is also observed during reduction of manganese dioxide to manganese oxyhydroxide in the vicinity of ORR region, the Mn–O bonds in the MnO₆ octahedra are forced to form a distorted Mn³⁺O₆ octahedron (four short and two long Mn–O bonds). These changes are attributed to Jahn–Teller distortion and hydrogen-bonding.⁷⁴ It is worth mentioning here that even in the case of the distortions directed by the Jahn–Teller effect and hydrogen bonding into the manganese oxyhydroxide, the overall structure of this compound does not change significantly from the native manganese dioxide structure.⁷⁴ The effects of structural defects into the electrochemical and adsorptive properties of several commercial manganese dioxides and the influence into the ORR in concentrated KOH aqueous solution have been reported in the work of Gyenge and Drillet.⁷⁵

Taken into account the above literature reports, we intended to correlate our X-ray absorption spectral information regarding the bond distances measured for different MnO₂ nanoshapes with their observed ORR catalytic activity. In the case of α -MnO₂ nanowires and nanoparticles, we have observed that the four Mn–O1 bond distance values has slightly been elongated and consequently two Mn–O2 bond distance become shortened with respect to bulk α -MnO₂ values. In contrast to this for other shapes, like, nanorods and nanoflowers, the two Mn–O2 bond distances become elongated when compared to bulk α -MnO₂ as shown in Table 2. Moreover, it is interesting to note that in all shapes, except for nanoflowers, the observed Mn–Mn distance values are greater than the bulk Mn–Mn distance of 2.819 Å. According to our electrocatalytic ORR observations, the α -MnO₂ nanowire catalyst displayed the lowest on-set potential, highest limiting current, and the *n*-value of 3.5 under similar experimental conditions. Such a behavior supports that the nanowire surface could provide a unique adsorption site for oxygen where two identical Mn sites exposing shortened Mn–O2 bonds protrude toward the oxygen molecule. It is worth noting that the distance between two Mn–Mn atoms are 1.824 Å, which could favor a bridge type adsorption of oxygen on the surface as shown in Scheme 1. However, in the case of nanoflower surfaces, both Mn–O2 and Mn–Mn distances are elongated, which may lead to the end-on

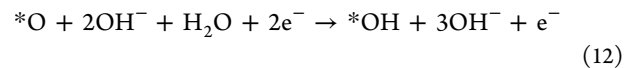
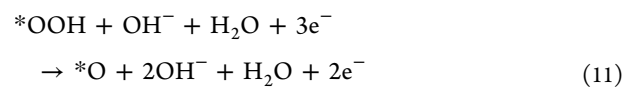
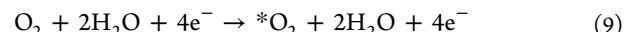
Scheme 1. Oxygen Molecule Adsorbed in a Horizontal Mode on Manganese Oxide Surface through a Bridge Type Configuration (Site A*) and an End-On Mode of Adsorption on Site B



or vertical mode of oxygen adsorption rather than bridge-type adsorption. Such circumstances produce a large quantity of peroxide as an intermediate, and eventually the *n*-value equals to 2. Our X-ray absorption studies finally uncovered a fact that the α -MnO₂ nanowire catalyst with two shortened Mn–O2 bonds along with a Mn–Mn distance of 2.819 Å < Mn–Mn distance < 2.825 Å acts co-operatively and provides an optimum requirement for the adsorbed oxygen in a bridge mode favoring the direct 4-electron reduction pathway.

The mass-transfer corrected kinetic current (i_k) _{$\omega \rightarrow 0$} derived at each potential from the Koutecky–Levich plot (Figure 9, panels A and B) along with geometric surface area of GC electrode are used to obtain the kinetic current densities (j_k) in order to construct Tafel plots for assessing specific activity at different potentials.⁶⁵ Tafel plots for the ORR on different MnO₂ catalyst surfaces shown in Figure 10C and their slope values are listed in Table 3. It can be realized that observed Tafel slope values lie between 60 and 120 mV decade⁻¹. It is interesting to note that in the case of nanowires and nanotubes, the slope value is 65 mV decade⁻¹, whereas for nanoflower, 115 mV decade⁻¹ is found. It may be due to the facile kinetics of oxygen reduction reaction on nanowires and nanotubes surfaces compared to the sluggish kinetics on nanoflower surfaces, which will be explained in the following section. Moreover, it should be mentioned that such kind of slope variations are also generally explained with respect to the change in the coverage degree of adsorbed oxygen.²⁶

3.5. Density Functional Theory Approach. The associative mechanism of oxygen reduction reaction in alkaline medium on the cathode α -MnO₂·0.25H₂O is studied in this work. The elementary steps of the reaction is



where * implies that the molecule is adsorbed on the surface of the cathode material. The α -MnO₂ crystallizes into tetragonal structure with lattice constants of $a = b = 9.77$ Å, and $c = 2.84$ Å. It is (2 × 2) tunnel structure, which has the ability to occupy

water molecules used during the synthesis process of the material. From our calculations, we confirmed that compound $\alpha\text{-MnO}_2\cdot x\text{H}_2\text{O}$ is stable when $x = 0.25$, by varying the concentration of the water molecules from $x = 0.0$ to 0.375 . When one more water molecule than $x = 0.25$ is added in the tunnel, the crystal network is collapsed. The optimized surfaces (110), (200), (211), and (310) of $\alpha\text{-MnO}_2\cdot 0.25\text{H}_2\text{O}$ are shown in Figure 11A. Various ORR intermediate species such as O_2 ,

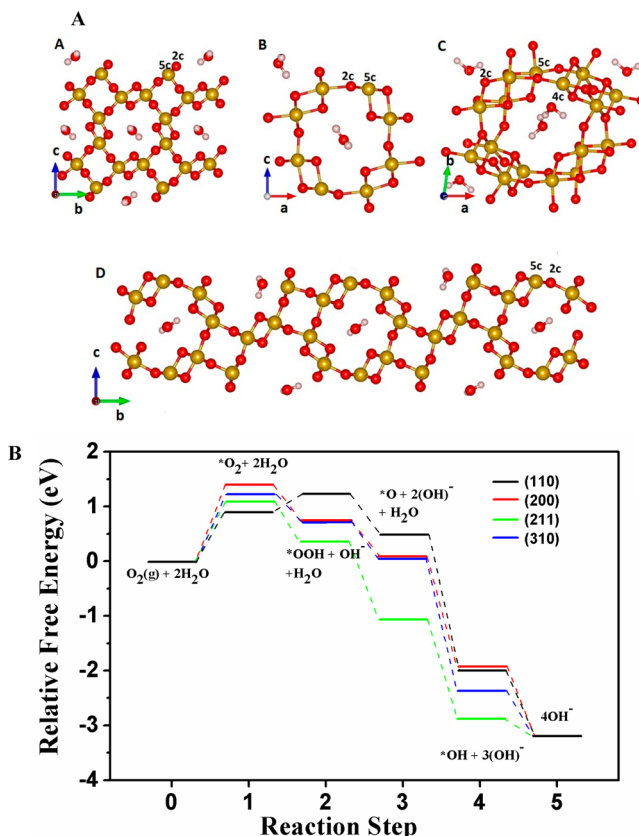


Figure 11. (A) Ball and stick model of optimized structure of (A) (110), (B) (200), (C) (211), and (D) (310) surface slabs of the $\alpha\text{-MnO}_2\cdot 0.25\text{H}_2\text{O}$ compound. Under-coordinated atoms are shown with their coordination. Yellow, red, and pale white balls correspond to Mn, O, and H atoms, respectively. (B) Free energies of different surface slabs of the $\alpha\text{-MnO}_2\cdot 0.25\text{H}_2\text{O}$ compound are shown for various intermediate steps involved in ORR.

O , OH , and OOH are allowed to interact with the surface of $\alpha\text{-MnO}_2\cdot 0.25\text{H}_2\text{O}$, and the adsorption energies are calculated from

$$E_{\text{ads}} = E_{\text{total}} - (E_{\text{as cleaved}} + E_{\text{species}})$$

where E_{ads} is the adsorption energy and E_{total} , $E_{\text{as cleaved}}$, and E_{species} are the total energy of the surface containing the adsorbate, of the corresponding clean surface, and of an isolated intermediate species, respectively. The change in free energy of a reaction is calculated from

$$\Delta G = \Delta E - T\Delta S + \Delta G_U + \Delta G_{\text{pH}}$$

where ΔE is the reaction energy (obtained using DFT calculations), ΔS is the change in the entropy (obtained from the thermodynamic data related to $T = 298$ K in ref 76), $\Delta G_U = -eU$, where e is the electrons involved in the reaction, U is the

electrode potential. Here, our interested potential is 0.141 V versus SHE obtained from the experimental electrochemical studies described above, and $\Delta G_{\text{pH}} = -k_B T \ln[H^+] = k_B T \ln 10 \times \text{pH}$. Here the pH used is 13 since the electrolyte is 0.1 M KOH. The change in zero-point energy is not taken into consideration because of its marginal effect on the free-energy profile.

The (110), (200), and (310) surfaces have Mn(5c) and O(2c) atoms on the surfaces, and the adsorbates such as O_2 , OOH , O , OH interacts with the Mn(5c) (optimized structure are shown in the Supporting Information), while the (211) surface has both Mn(5c) and Mn(4c) atoms, apart from O(2c) atoms. Thus, adsorbate prefers to interact with the Mn(4c). The adsorption energies are calculated and shown in Table 4, it

Table 4. Adsorption Energy (E_{ads} in eV) of Different Adsorbate on (110), (200), (211), and (310) Surfaces of $\alpha\text{-MnO}_2\cdot 0.25\text{H}_2\text{O}$ Compounds

	O	OH	OOH	O_2
(110)	-1.984	-2.167	-0.473	-0.039
(200)	-2.384	-2.125	-0.984	0.136
(211)	-3.528	-3.063	-1.342	-0.159
(310)	-2.406	-2.537	-0.975	-0.032

implies that the interaction between the surface and adsorbates is stronger for the (211) surface than all other surfaces. Our calculations show that the O and OOH adsorption is less feasible for (110), while the O_2 , OH adsorption is less feasible for (200) surface.

The free-energy profile for those different surfaces of $\alpha\text{-MnO}_2\cdot 0.25\text{H}_2\text{O}$ is shown in Figure 11B. The free energies of the reaction intermediates were calculated relative to $\text{O}_2 + 2\text{H}_2\text{O}$. Overall picture shows that the ORR on $\alpha\text{-MnO}_2\cdot 0.25\text{H}_2\text{O}$ is exergonic. It also shows that for the (110) surface, adsorption of O_2 and reduction toward OOH are uphill and all others are downhill in energy, so the rate-determining step is the reduction toward OOH . For the (200), (211), and (310) surfaces, the rate-determining step is adsorption of O_2 , since it is uphill and all other steps are downhill. All the surfaces need energy for O_2 adsorption. The activation barrier for (200), (211), and (310) (adsorption of O_2) is 1.395, 1.089, 1.230 eV, respectively. For (110), the activation barrier (reduction toward OOH) is 1.236 eV. Compared to other surfaces, ORR happens more feasibly on (211) and is least on (200).

CONCLUSIONS

In summary, we report an environmental benign, cost-effective, and phase pure synthesis of shape-designed MnO_2 materials in five distinct morphologies. All the five materials were obtained with remarkable crystallographic purity, appreciable morphological homogeneity. The observed manganese oxidation states were found identical with a slight change in their oxygen environments due to geometry effects. All the shapes of MnO_2 have shown attractive catalytic activity toward oxygen reduction reactions in alkaline medium. Our results show that the electrocatalytic activities are greatly dependent on the nano-shapes, in the following order nanowire > nanorod > nanotube > nanoparticle > nanoflower. $\alpha\text{-MnO}_2$ nanowires possess enhanced electrocatalytic activity in terms of more positive on-set potential and highest diffusion limiting current compared to other shapes, even though the nanotubes possess a much higher BET surface area. The kinetic studies reveal that

the Tafel slope value 65 mV/decade, K-L plots yields a 4e⁻ transfer for α -MnO₂ nanowire, while other shapes have 2e⁻ transfer. In addition, α -MnO₂ nanowire produces 3.6% of hydrogen peroxide production during ORR. The superior ORR activity was attributed to the fact that it possesses active sites composed with two shortened Mn–O bonds along with a Mn–Mn distance of 2.824 Å, which provides (plays co-operatively) an optimum requirement for the adsorbed oxygen in a bridge mode favoring the direct 4 electron reduction. It is proposed that such kind of structural phenomenon originated from the nanogeometry effect, whereas α -MnO₂ nanoparticle surfaces encourages the partial reduction of oxygen to peroxide on one active site and peroxide reduction on another site which reflected in its lower *n* value observed in our study. The α -MnO₂ nanowire catalyst may be enriched by the (211) crystallographic planes, where the decomposition of reaction intermediates are energetically favored as proved by DFT calculations.

ASSOCIATED CONTENT

Supporting Information

Figure S1–S6 include information for IR spectra, BET isotherms, EDX spectra, Mn K-edge pre-edge plot, RDE voltammograms for different MnO₂ samples, and ball and stick model of optimized structure of (110) surface slab with the reaction intermediates as adsorbates. This material is available free of charge via the Internet at <http://pubs.acs.org>.

AUTHOR INFORMATION

Corresponding Author

*E-mail: senthilecms@gmail.com and senthilkumarsm@cecri.res.in.

Notes

The authors declare no competing financial interest.

ACKNOWLEDGMENTS

The authors appreciate the financial support from CSIR through 12th FYP project MULTIFUN (CSC 0101). We would like to thank our Director, Dr. Vijayamohanan K. Pillai, for his constant support and suggestions. The authors also thank the staff members of Central Instrument Facility of CSIR-CECRI for their tremendous help and valuable contributions. We would like to thank Dr. K. L. N. Phani for allowing us to use their Ivium BiPot instrument. We also thank Prof. K. Chandrasekara Pillai for his constant support and guidance. Calculations were carried out at CSIR-CECRI's high-performance computing facility. K.G. is grateful to DST for providing an INSPIRE fellowship.

REFERENCES

- (1) Gong, K.; Du, F.; Xia, Z.; Durstock, M.; Dai, L. Nitrogen-Doped Carbon Nanotube Arrays with High Electrocatalytic Activity for Oxygen Reduction. *Science* **2009**, *323*, 760–764.
- (2) Lefevre, M.; Proietti, E.; Jaouen, F.; Dodelet, J. P. Iron-Based Catalysts with Improved Oxygen Reduction Activity in Polymer Electrolyte Fuel Cells. *Science* **2009**, *324*, 71–74.
- (3) Lim, B.; Jiang, M.; Camargo, P. H. C.; Cho, E. C.; Tao, J.; Lu, X.; Zhu, Y.; Xia, Y. Pd-Pt Bimetallic Nanodendrites with High activity for Oxygen Reduction. *Science* **2009**, *324*, 1302–1305.
- (4) Winther-Jensen, B.; Winther-Jensen, O.; Forsyth, M.; Macfarlane, D. R. High Rates of Oxygen Reduction over a Vapor Phase-Polymerized PEDOT Electrode. *Science* **2008**, *321*, 671–674.
- (5) Spendelow, J. S.; Wieckowski, A. Electrocatalysis of Oxygen Reduction and Small Alcohol Oxidation in Alkaline Media. *Phys. Chem. Chem. Phys.* **2007**, *9*, 2654–2675.
- (6) Chen, W.; Chen, S. Oxygen Electroreduction Catalyzed by Gold Nanoclusters: Strong Core Size Effects. *Angew. Chem., Int. Ed.* **2009**, *48*, 4386–4389.
- (7) Chen, Z.; Waje, M.; Li, W.; Yan, Y. Supportless Pt and PtPd Nanotubes as Electrocatalysts for Oxygen-Reduction Reactions. *Angew. Chem., Int. Ed.* **2007**, *46*, 4060–4063.
- (8) Xiao, L.; Zhuang, L.; Liu, Y.; Lu, J.; Abruna, H. D. Activating Pd by Morphology Tailoring for Oxygen Reduction. *J. Am. Chem. Soc.* **2009**, *131*, 602–608.
- (9) Wang, C.; Daimon, H.; Sun, S. Dumbbell-Like Pt–Fe₃O₄ Nanoparticles and Their Enhanced Catalysis for Oxygen Reduction Reaction. *Nano Lett.* **2009**, *9*, 1493–1496.
- (10) Bashyam, R.; Zelenay, P. A Class of Non-precious Metal Composite Catalysts for Fuel Cells. *Nature* **2006**, *443*, 63–66.
- (11) Zhou, Q.; Li, C. M.; Li, J.; Lu, J. Electrocatalysis of Template-Electrosynthesized Cobalt–Porphyrin/Polyaniline Nanocomposite for Oxygen Reduction. *J. Phys. Chem. C* **2008**, *112*, 18578–18583.
- (12) Crisostomo, V. M. B.; Ngala, J. K.; Alia, S.; Dobley, A.; Morein, C.; Chen, C. H.; Shen, X. F.; Suib, S. L. New Synthetic Route, Characterization, and Electrocatalytic Activity of Nanosized Manganese. *Chem. Mater.* **2007**, *19*, 1832–1839.
- (13) Liu, Z.; Xing, Y.; Chen, C. H.; Zhao, L.; Suib, S. L. Framework Doping of Indium in Manganese Oxide Materials: Synthesis, Characterization, and Electrocatalytic Reduction of Oxygen. *Chem. Mater.* **2008**, *20*, 2069–2071.
- (14) Wang, Y. G.; Cheng, L.; Li, F.; Xiong, H. M.; Xia, Y. Y. High Electrocatalytic Performance of Mn₃O₄/Mesoporous Carbon Composite for Oxygen Reduction in Alkaline Solutions. *Chem. Mater.* **2007**, *19*, 2095–2101.
- (15) Shanmugam, S.; Gedanken, A. MnO Octahedral Nanocrystals and MnO@C Core–Shell Composites: Synthesis, Characterization, and Electrocatalytic Properties. *J. Phys. Chem. B* **2006**, *110*, 24486–24491.
- (16) Gong, K.; Yu, P.; Su, L.; Xiong, S.; Mao, L. Polymer-Assisted Synthesis of Manganese Dioxide/Carbon Nanotube Nanocomposite with Excellent Electrocatalytic Activity Toward Reduction of Oxygen. *J. Phys. Chem. C* **2007**, *111*, 1882–1887.
- (17) Roche, I.; Chainet, E.; Chatenet, M.; Vondrak, J. Carbon-Supported Manganese Oxide Nanoparticles as Electrocatalysts for the Oxygen Reduction Reaction (ORR) in Alkaline Medium: Physical Characterizations and ORR Mechanism. *J. Phys. Chem. C* **2007**, *111*, 1434–1443.
- (18) Cao, Y. L.; Yang, H. X.; Ai, X. P.; Xiao, L. F. The Mechanism of Oxygen Reduction on MnO₂-Catalyzed Air Cathode in Alkaline Solution. *J. Electroanal. Chem.* **2003**, *557*, 127–134.
- (19) Lima, F. H. B.; Calegaro, M. L.; Ticianelli, E. A. Electrocatalytic Activity of Manganese Oxides Prepared by Thermal Decomposition for Oxygen Reduction. *Electrochim. Acta* **2007**, *52*, 3732–3738.
- (20) Hu, F. P.; Zhang, X. G.; Xiao, F.; Zhang, J. L. Oxygen Reduction on Ag–MnO₂/SWNT and Ag–MnO₂/AB Electrodes. *Carbon* **2005**, *43*, 2931–2936.
- (21) Debart, A.; Paterson, A. J.; Bao, J.; Bruce, P. G. α -MnO₂ Nanowires: A Catalyst for the O₂ Electrode in Rechargeable Lithium Batteries. *Angew. Chem., Int. Ed.* **2008**, *47*, 4521–4524.
- (22) Lu, S.; Pan, J.; Huang, A.; Zhuang, L.; Lu, J. Alkaline Polymer Electrolyte Fuel Cells Completely Free from Noble Metal Catalysts. *Proc. Natl. Acad. Sci. U.S.A.* **2008**, *105*, 20611–20614.
- (23) Klapste, B.; Vondrak, J.; Velicka, J. MnO_x/C Composites as Electrode Materials II. Reduction of Oxygen on Bifunctional Catalysts Based on Manganese Oxides. *Electrochim. Acta* **2002**, *47*, 2365–2369.
- (24) El-Deab, M. S.; Ohsaka, T. Manganese Oxide Nanoparticles Electrodeposited on Platinum Are Superior to Platinum for Oxygen Reduction. *Angew. Chem., Int. Ed.* **2006**, *45*, 5963–5966.
- (25) Ohsaka, T.; Mao, L.; Arihara, K.; Sotomura, T. Bifunctional Catalytic Activity of Manganese Oxide Toward O₂ Reduction: Novel

- Insight into The Mechanism of Alkaline Air Electrode. *Electrochim. Commun.* **2004**, *6*, 273–277.
- (26) Lima, F. H. B.; Calegaro, M. L.; Ticianelli, E. A. Investigations of the Catalytic Properties of Manganese Oxides for The Oxygen Reduction Reaction in Alkaline Media. *J. Electroanal. Chem.* **2006**, *590*, 152–160.
- (27) Mao, L.; Zhang, D.; Sotomura, T.; Nakatsu, K.; Koshiba, N.; Ohsaka, T. Mechanistic Study of The Reduction of Oxygen in Air Electrode with Manganese Oxides as Electrocatalysts. *Electrochim. Acta* **2003**, *48*, 1015–1021.
- (28) Verma, A.; Jha, A. K.; Basu, S. Manganese Dioxide as A Cathode Catalyst for A Direct Alcohol or Sodium Borohydride Fuel Cell with a Flowing Alkaline Electrolyte. *J. Power Sources* **2005**, *141*, 30–34.
- (29) Yang, J.; Xu, J. J. Nanoporous Amorphous Manganese Oxide as Electrocatalyst for Oxygen Reduction in Alkaline Solutions. *J. Electrochim. Commun.* **2003**, *5*, 306–311.
- (30) Cheng, F.; Su, Y.; Liang, J.; Tao, Z.; Chen, J. MnO₂-Based Nanostructures as Catalysts for Electrochemical Oxygen Reduction in Alkaline Media. *Chem. Mater.* **2010**, *22*, 898–905.
- (31) Xiao, W.; Wang, D.; Lou, X. W. Shape-Controlled Synthesis of MnO₂ Nanostructures with Enhanced Electrocatalytic Activity for Oxygen Reduction. *J. Phys. Chem. C* **2010**, *114*, 1694–1700.
- (32) Suib, S. L. Porous Manganese Oxide Octahedral Molecular Sieves and Octahedral Layered Materials. *Acc. Chem. Res.* **2008**, *41*, 479–487.
- (33) Seo, W. S.; Jo, H. H.; Lee, K.; Kim, B.; Oh, S. J.; Park, J. T. Size-Dependent Magnetic Properties of Colloidal Mn₃O₄ and MnO Nanoparticles. *Angew. Chem., Int. Ed.* **2004**, *43*, 1115–1117.
- (34) Cheng, F. Y.; Chen, J.; Gou, X. L.; Shen, P. W. High-Power Alkaline Zn–MnO₂ Batteries Using γ -MnO₂Nanowires/Nanotubes and Electrolytic Zinc Powder. *Adv. Mater.* **2005**, *17*, 2753–2756.
- (35) Cheng, F.; Zhao, J.; Song, W.; Li, C.; Ma, H.; Chen, J.; Shen, P. Facile Controlled Synthesis of MnO₂ Nanostructures of Novel Shapes and Their Application in Batteries. *Inorg. Chem.* **2006**, *45*, 2038–2044.
- (36) Devaraj, S.; Munichandraiah, N. Effect of Crystallographic Structure of MnO₂ on Its Electrochemical Capacitance Properties. *J. Phys. Chem. C* **2008**, *112*, 4406–4417.
- (37) Meng, Y.; Song, W.; Huang, H.; Ren, Z.; Chen, S. Y.; Suib, S. L. Structure–Property Relationship of Bifunctional MnO₂ Nanostructures: Highly Efficient, Ultra-Stable Electrochemical Water Oxidation and Oxygen Reduction Reaction Catalysts Identified in Alkaline Media. *J. Am. Chem. Soc.* **2014**, *136*, 11452–11464.
- (38) Boppana, V. B. R.; Jiao, F. Nanostructured MnO₂: An Efficient and Robust Water Oxidation Catalyst. *Chem. Commun.* **2011**, *47*, 8973–8975.
- (39) Xia, H.; Wang, Y.; Lin, J.; Lu, L. Hydrothermal Synthesis of MnO₂/CNT Nanocomposite with a CNT Core/Porous MnO₂ Sheath Hierarch Architecture for Supercapacitors. *Nanoscale Res. Lett.* **2012**, *7*, 33–42.
- (40) Yan, D.; Yan, P. X.; Yue, G. H.; Liu, J. Z.; Chang, J. B.; Yang, Q.; Qu, D. M.; Geng, Z. R.; Chen, J. T.; Zhang, G. A.; et al. Self-Assembled Flower-Like Hierarchical Spheres and Nanobelts of Manganese Oxide by Hydrothermal Method and Morphology Control of them. *Chem. Phys. Lett.* **2007**, *440*, 134–138.
- (41) Johnson, C. S.; Dees, D. W.; Mansuetto, M. F.; Thackeray, M. M.; Vissers, D. R.; Argyriou, D.; Loong, C. K.; Christensen, L. Structural and Electrochemical Studies of α -Manganese Dioxide (α -MnO₂). *J. Power Sources* **1997**, *68*, 570–577.
- (42) Zabinsky, S. I.; Rehr, J. J.; Ankudinov, A.; Albers, R. C.; Eller, M. J. Multiple-Scattering Calculations of X-ray-Absorption Spectra. *J. Phys. Rev. B* **1995**, *52*, 2995–3009.
- (43) Ravel, B.; Newville, M. Athena, Artemis, Hephaestus: data Analysis for X-ray Absorption Spectroscopy using Ifeffit. *J. Synchrotron Radiat.* **2005**, *12*, 537–541.
- (44) Kresse, G.; Joubert, D. From Ultrasoft Pseudopotentials to The Projector Augmented-Wave Method. *Phys. Rev. B: Condens. Matter Mater. Phys.* **1999**, *59*, 1758–1775.
- (45) Blochl, P. E. Projector Augmented-Wave Method. *Phys. Rev. B: Condens. Matter Mater. Phys.* **1994**, *50*, 17953–17979.
- (46) Perdew, J. P.; Chevary, J. A.; Vosko, S. H.; Jackson, K. A.; Pederson, M. R.; Singh, D. J.; Fiolhais, C. Atoms, Molecules, Solids, and Surfaces: Applications of The Generalized Gradient Approximation for Exchange and Correlation. *Phys. Rev. B: Condens. Matter Mater. Phys.* **1992**, *46*, 6671–6687.
- (47) Cheng, F.; Zhang, T.; Zhang, Y.; Du, J.; Han, X.; Chen, J. Enhancing Electrocatalytic Oxygen Reduction on MnO₂ with Vacancies. *Angew. Chem.* **2013**, *125*, 2534–2537.
- (48) Sui, N.; Duan, Y.; Jiao, X.; Chen, D. Large-Scale Preparation and Catalytic Properties of One-Dimensional α / β -MnO₂ Nanostructures. *J. Phys. Chem. C* **2009**, *113*, 8560–8565.
- (49) Ma, R.; Bando, Y.; Zhang, L.; Sasaki, T. Layered MnO₂ Nanobelts: Hydrothermal Synthesis and Electrochemical Measurements. *Adv. Mater.* **2004**, *16*, 918–922.
- (50) Kang, L.; Zhang, M.; Liu, Z. H.; Ooi, K. IR Spectra of Manganese Oxides with Either Layered or Tunnel Structures. *Spectrochim. Acta, Part A* **2007**, *67*, 864–869.
- (51) Li, Y.; Wang, J.; Zhang, Y.; Banis, M. N.; Liu, J.; Geng, D.; Li, R.; Sun, X. Facile Controlled Synthesis and Growth Mechanisms of Flower-Like and Tubular MnO₂ Nanostructures by Microwave-Assisted Hydrothermal Method. *J. Colloid Interface Sci.* **2012**, *369*, 123–128.
- (52) Gao, T.; Fjellvag, H.; Norby, P. A Comparison Study on Raman Scattering Properties of α - and β -MnO₂. *Anal. Chim. Acta* **2009**, *648*, 235–239.
- (53) Luo, J.; Zhu, H. T.; Fan, H. M.; Liang, J. K.; Shi, H. L.; Rao, G. H.; Li, J. B.; Du, Z. M.; Shen, Z. X. Synthesis of Single-Crystal Tetragonal α -MnO₂ Nanotubes. *J. Phys. Chem. C* **2008**, *112*, 12594–12598.
- (54) Zhang, J.; Jiang, J.; Zhao, X. S. Synthesis and Capacitive Properties of Manganese Oxide Nanosheets Dispersed on Functionalized Graphene Sheets. *J. Phys. Chem. C* **2011**, *115*, 6448–6454.
- (55) Subramanian, V.; Zhu, H.; Vajtai, R.; Ajayan, P. M.; Wei, B. Hydrothermal Synthesis and Pseudocapacitance Properties of MnO₂ Nanostructures. *J. Phys. Chem. B* **2005**, *109*, 20207–20214.
- (56) Li, B.; Rong, G.; Xie, Y.; Huang, L.; Feng, C. Low-Temperature Synthesis of α -MnO₂ Hollow Urchins and Their Application in Rechargeable Li⁺ Batteries. *Inorg. Chem.* **2006**, *45*, 6404–6410.
- (57) McIntyre, N. S.; Zetaruk, D. G. X-ray Photoelectron Spectroscopic Studies of Iron Oxides. *Anal. Chem.* **1977**, *49*, 1521–1529.
- (58) Masquelier, C.; Tabuchi, M.; Ado, K.; Kanno, R.; Kobayashi, Y.; Maki, Y.; Nakamura, O.; Goodenough, J. B. Chemical and Magnetic Characterization of Spinel Materials in the LiMn₂O₄–Li₂Mn₄O₉–Li₄Mn₅O₁₂ System. *J. Solid State Chem.* **1996**, *123*, 255–266.
- (59) Stoyanova, R.; Gorova, M.; Zhecheva, E. EPR of Mn⁴⁺ in Spinels Li_{1+x}Mn_{2-x}O₄ with 0 ≤ x ≤ 0.1. *J. Phys. Chem. Solids* **2000**, *61*, 609–614.
- (60) Stoyanova, R.; Gorova, M.; Zhecheva, E. EPR Monitoring of Mn⁴⁺ Distribution in Li₄Mn₅O₁₂ Spinels. *J. Phys. Chem. Solids* **2000**, *61*, 615–620.
- (61) Chen, Z.; Jiao, Z.; Pan, D.; Li, Z.; Wu, M.; Shek, C. H.; Wu, C. M. L.; Lai, J. K. L. Recent Advances in Manganese Oxide Nanocrystals: Fabrication, Characterization, and Microstructure. *Chem. Rev.* **2012**, *112*, 3833–3855.
- (62) El-Sawy, A. M.; King'ondu, C. K.; Kuo, C. H.; Kriz, D. A.; Guild, C. J.; Meng, Y.; Frueh, S. J.; Dharmaratna, S.; Ehrlich, S. N.; Suib, S. L. X-ray Absorption Spectroscopic Study of a Highly Thermally Stable Manganese Oxide Octahedral Molecular Sieve (OMS-2) with High Oxygen Reduction Reaction Activity. *Chem. Mater.* **2014**, *26*, 5752–5760.
- (63) Kijima, N.; Ikeda, T.; Oikawa, K.; Izumi, F.; Yoshimura, Y. Crystal Structure of An Open-Tunnel Oxide α -MnO₂ Analyzed by Rietveld Refinements and MEM-Based Pattern Fitting. *J. Solid State Chem.* **2004**, *177*, 1258–1267.
- (64) Post, J. E.; Von Dreele, R. B.; Buseck, P. R. Symmetry and Cation Displacements in Hollandite, cryptomelane and priderite. *Acta Crystallogr., Sect. B* **1982**, *38*, 1056–1065.

- (65) Anastasijevic, N. A.; Vesovic, V.; Adzic, R. R. Determination of Kinetic Parameters of The Oxygen Reduction Reaction using The Rotating Ring-Disk Electrode, Part I: Theory. *J. Electroanal. Chem.* **1987**, *229*, 305–316.
- (66) Adzic, R. Frontiers in Electrochemistry. In *Electrocatalysis*; Wiley-VCH: New York, 1998.
- (67) Stamenkovic, V.; Schmidt, T. J.; Ross, P. N.; Markovic, N. M. Surface Composition Effects in Electrocatalysis: Kinetics of Oxygen Reduction on Well-Defined Pt₃Ni and Pt₃Co Alloy Surfaces. *J. Phys. Chem. B* **2002**, *106*, 11970–11979.
- (68) Mamlouk, M.; Senthil Kumar, S. M.; Gouerec, P.; Scott, K. Electrochemical and Fuel Cell Evaluation of Co Based Catalyst for Oxygen Reduction in Anion Exchange Polymer Membrane Fuel Cells. *J. Power Sources* **2011**, *196*, 7594–7600.
- (69) Gorlin, Y.; Chung, C. J.; Nordlund, D.; Clemens, B. M.; Jaramillo, T. F. Mn₃O₄ Supported on Glassy Carbon: An Active Non-Precious Metal Catalyst for the Oxygen Reduction Reaction. *ACS Catal.* **2012**, *2*, 2687–2694.
- (70) Yeager, E. Dioxygen Electrocatalysis: Mechanisms in Relation to Catalyst Structure. *J. Mol. Catal.* **1986**, *38*, 5–25.
- (71) Roche, I.; Chainet, E.; Chatenet, M.; Vondrak, J. Carbon-Supported Manganese Oxide Nanoparticles as Electrocatalysts for the Oxygen Reduction Reaction (ORR) in Alkaline Medium: Physical Characterizations and ORR Mechanism. *J. Phys. Chem. C* **2007**, *111*, 1434–1443.
- (72) Kwon, K. D.; Refson, K.; Sposito, G. Defect-Induced Photoconductivity in Layered Manganese Oxides: A Density Functional Theory Study. *Phys. Rev. Lett.* **2008**, *100*, 146601–146604.
- (73) Ruetschi, P. Cation-Vacancy Model for MnO₂. *J. Electrochem. Soc.* **1984**, *131*, 2737–2744.
- (74) Kohler, T.; Armbruster, T.; Libowitzky, E. Hydrogen Bonding and Jahn–Teller Distortion in Groutite, α -MnOOH, and Manganite, γ -MnOOH, and Their Relations to the Manganese Dioxides Ramsdellite and Pyrolusite. *J. Solid State Chem.* **1997**, *133*, 486–500.
- (75) Gyenge, E. L.; Drillet, J. F. The Electrochemical Behavior and Catalytic Activity for Oxygen Reduction of MnO₂/C– Toray Gas Diffusion Electrodes. *J. Electrochem. Soc.* **2012**, *159*, F23–F34.
- (76) Atkins, P. W. *Physical Chemistry*, 6th ed.; Oxford University Press: Oxford, U.K., 1998.